In situ observation of the interfacial lattice reconstruction in $SrRuO_3/SrTiO_3$ heterostructures driven by the $SrTiO_3$ phase transition

Pengxian You,[1,2,3,*] Junhong Yu,[2,3,*] Jing Yang,[2,3] Hang Zhang,[2,3] Min Liao,[1,†] and Jianbo Hu[2,3,‡]

[1]*School of Materials Science and Engineering, Xiangtan University, Xiangtan 411105, China*

[2]*Laboratory for Shock Wave and Detonation Physics, Institute of Fluid Physics, China Academy of Engineering Physics, Mianyang 621900, China*

[3]*State Key Laboratory for Environment-Friendly Energy Materials, Southwest University of Science and Technology, Mianyang 621010, China*

(Received 22 July 2023; revised 14 November 2023; accepted 27 November 2023; published 26 December 2023)

The change in physical properties of epitaxial $SrRuO_3/SrTiO_3$ (SRO/STO) heterostructures occurring at the STO phase-transition temperature of 105 K has attracted enormous research interest. In this work, we have investigated the interfacial lattice structures in the SRO/STO heterostructure below and above 105 K. Based on the high-resolution structural analysis and ultrafast x-ray-diffraction experiments, we have revealed an interfacial lattice reconstruction of the SRO layer both in the real space and reciprocal space. Such an interfacial lattice reconstruction can be attributed to the cubic-to-tetragonal transition that occurs in structural transitions of the STO substrate.

DOI: 10.1103/PhysRevB.108.224113

I. INTRODUCTION

Due to strong couplings among spin, charge, and orbital degrees of freedom at the interface, the epitaxial growth of complex perovskite transition-metal oxides (ABO_3) can create emergent quantum states that do not exist in their parent compounds. For instance, the quasi-2D electron gas and low-temperature superconducting state emerge at the $LaAlO_3/SrTiO_3$ heterointerface [1]. In strained $SrTiO_3$ films, ferroelectricity is observed [2], and in the $PbTiO_3/SrTiO_3$ superlattices, vortices form [3]. The lattice mismatch between the $SrRuO_3$ (SRO, a pseudocubic structure with a lattice parameter of 0.393 nm) epitaxial film and the $SrTiO_3$ (STO, a standard cubic structure with a lattice parameter of 0.3905 nm) substrate is nearly perfect, making the SRO/STO heterostructure one of the best perovskite-oxide combinations reported so far [4]. Recently, SRO heterostructures have shown great potential application in quantum information storage and logic devices due to the discovery of the topological Hall effect [5,6], chiral spin fluctuation [7], and skyrmion [8].

The physical property of STO-based heterostructures, such as magnetism and electrical conductivity, undergoes an abrupt change at $\sim$ 105 K and the physical origin of this change is under debate [9–11]. However, the coincidence of the cubic-to-tetragonal phase transition of the STO substrate at the same temperature [12–14] suggests that the exotic transport properties at $T = 105$ K may relate to the STO-induced interfacial lattice reconstruction. Given that SRO's electronic structure is highly sensitive to tilts and rotations of the oxygen octahedron due to the strong hybridization between Ru *4d* orbitals and O *2p* orbitals [15], the phase transition in the STO substrate is expected to alter the octahedral geometry in the SRO film, thus changing the coupling status of spins and charges at the interface.

To verify this speculation, we provide atomic-scale structural information on the octahedral behavior at the SRO/STO heterointerface and uncover the related microscopic mechanism of substrate-induced interfacial reconstruction in this work. By using the spherical aberration-corrected transmission electron microscope (TEM), we observe a localized RuO_6 octahedral distortion emerging in the near-interface region of the SRO film at room temperature (300 K) after the STO phase transition. This distortion results in a pronounced RuO_6 octahedral tilting relative to the original orthorhombic phase. To further analyze the interface lattice reconstruction, ultrafast x-ray diffraction (UXRD) is introduced to track the lattice dynamics of SRO/STO heterostructures at the temperature below (80 K) and above (300 K) the STO phase transition. The split SRO (200) Bragg peak at 80 K and the reduced characteristic time of the photoacoustic wave at 80 K unambiguously indicate the formation of a two-layered structure in SRO, which is attributed to the phase transition of the STO substrate below 105 K that enhances the lattice symmetry mismatch.

II. RESULT AND DISCUSSION

A high-quality SRO epitaxial single-crystal film is deposited on (100) STO substrate using molecular-beam epitaxy. Detailed lattice structures of the SRO film and the STO substrate are presented in Fig. S1 [16]. As shown in Fig. 1(a), the *in situ* static XRD is performed by utilizing a homemade laser-driven plasma femtosecond x-ray source (PXS) [20] in the absence of the laser pump beam. The temperature variations were as follows: 300 K (pristine state), 80, and 300 K (with

*These authors contributed equally to this work.
†mliao@xtu.edu.cn
‡jianbo.hu@caep.cn

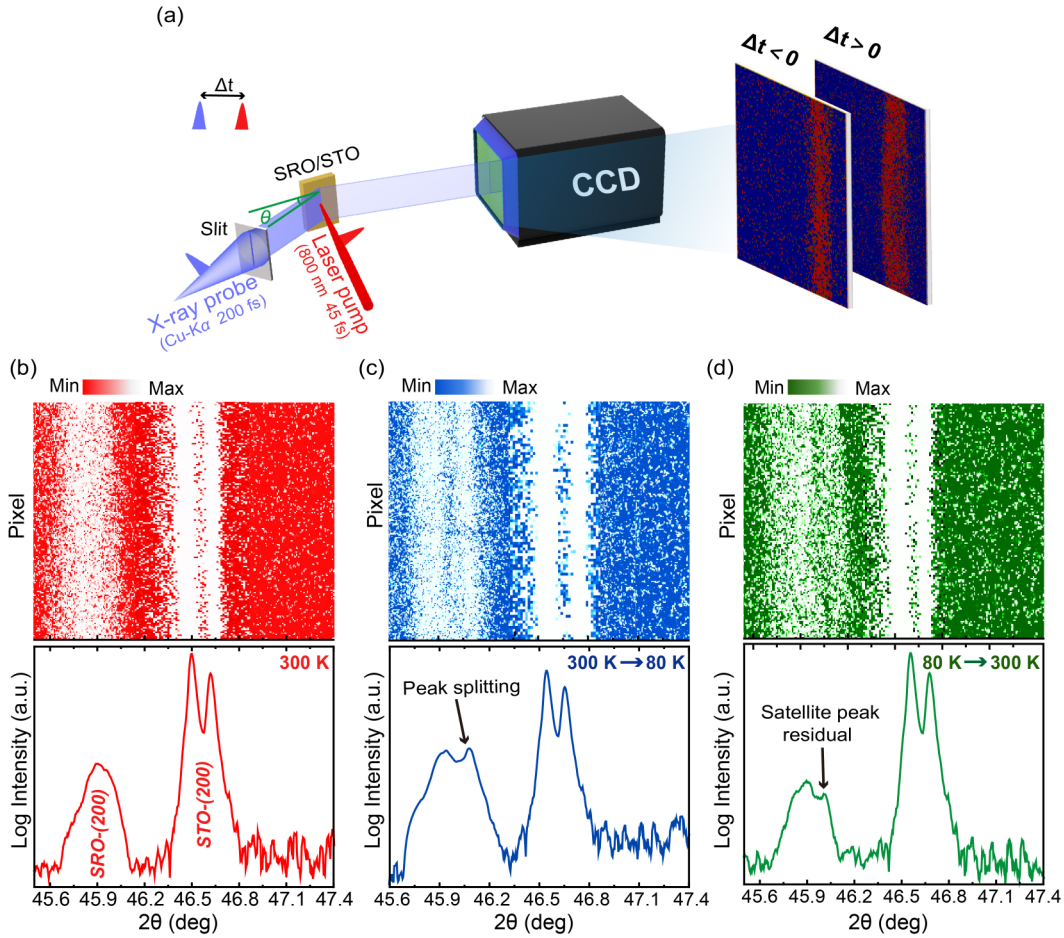

FIG. 1. Static XRD measurements of the SRO/STO heterostructure. (a) Ultrafast x-ray-diffraction experimental setup based on laser-driven plasma ultrafast x-ray source (PXS). Standard static x-ray scans are performed without the laser pump beam. (b) The SRO/STO (200) Bragg reflections measured at 300 K without any cooling history. (c) The SRO/STO (200) Bragg reflections measured at 80 K, which show an obvious splitting of the SRO-(200) Bragg peak. (d) The SRO/STO (200) Bragg reflections measured at 300 K with the cooling history. Upon increasing the temperature from 80 to 300 K, the satellite SRO-(200) Bragg peak at room temperature becomes weaker but still can be identified. The color maps are presented on a linear scale.

cooling history). By continuously changing the temperature with the setup of a cryogenic chamber, we can obtain the XRD patterns as shown in Figs. 1(b)–1(d), which present the (200) Bragg reflection of both SRO film and STO substrate under three different conditions. Note that the $\theta-2\theta$ scans obtained by PXS static scanning are consistent with those acquired with a standard diffractometer (see Fig. S2 in the Supplemental Material for the comparison) [16]. Figure 1(b) shows the $\theta-2\theta$ scans surrounding the respective (200) Bragg reflections of the pristine SRO/STO heterostructure measured at 300 K without any cooling history, which displays an intensive Voigt-like shape Bragg reflection [SRO - (200) at $2\theta = 45.93^\circ$], indicating the excellent epitaxial crystalline quality of the SRO film [21]. Interestingly, when the temperature falls below 105 K, the SRO-(200) Bragg peak bifurcates into two: one remains unchanged, while the other shifts to a larger angle at $2\theta = 46.05^\circ$ [see Fig. 1(c) measured at 80 K], suggesting a prominent lattice structure change. Furthermore, when heating the SRO/STO heterostructure from 80 to 300 K, the emerged SRO-(200) Bragg peak at $2\theta = 46^\circ$ becomes weaker but still can be resolved at room temperature, i.e., lattice changes in the SRO layer are not fully recovered when heating back to room temperature. To rule out strain relaxations simply due to thermal expansion during the cooling/heating cycle, static XRD data at 120 K (not cooled below 105 K) are presented, wherein no discernible peak-splitting behavior of the (200) Bragg reflections of the SRO-(200) Bragg peak is observed (see Fig. S3) [16]. These observations suggest that when the STO substrate undergoes the cubic-to-tetragonal phase transition at 105 K, the SRO layer probably consists of two regions with different lattice parameters along the vertical growth direction, leading to the splitting of the SRO-(200) Bragg peak. The residual change can even be retained at room temperature. In addition, we conducted static diffraction simulations at 80 K using lattice parameters obtained from TEM, and the results are in good agreement with the experimental data. (see Fig. S4) [16].

To verify the possible lattice structure changes of the SRO layer when the STO substrate undergoes the phase transition, the cross-section atomic position near the SRO/STO heterointerface has been imaged by the spherical aberration-corrected TEM. Figure 2(a) shows the cross-section TEM micrograph of the SRO/STO heterostructure at 300 K with the cooling history [i.e., corresponds to the case in Fig. 1(d)]. It shows

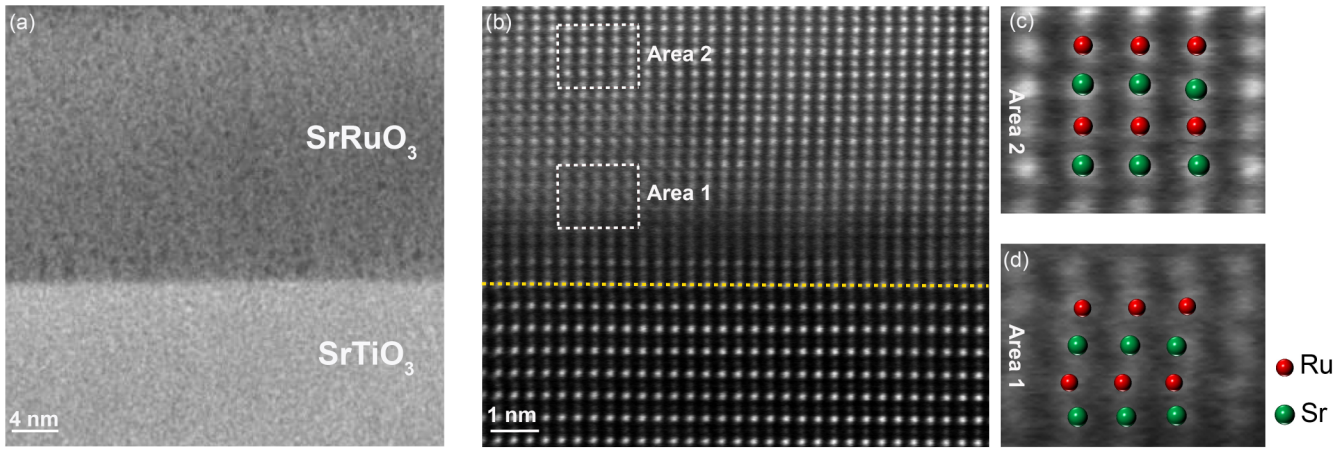

FIG. 2. Atomic-scale characterization across the $SrRuO_3/SrTiO_3$ interface with the cooling history. (a) Cross-section TEM image of the ∼ 76.6-nm SRO film grown on STO substrate; the scale bar is 4 nm. (b) High-resolution TEM image of atomic positions near the SRO/STO heterointerface. The yellow dashed line indicates the location of the heterointerface. Two distinct atomic areas are marked as area 1 and area 2, respectively. (c) The magnified image of area 2 away from the SRO/STO heterointerface. (d) The magnified image of area 1 is close to the SRO/STO heterointerface.

clearly that the SRO film has a flat surface and a sharp interface with a uniform thickness of ∼ 76.6 nm. Two distinct lattice structures of the SRO layer have been unambiguously identified at the atomic scale. As shown in Figs. 2(b) and 2(c), for the area far away from the heterointerface [indicated by the yellow dotted line in Fig. 2(b)], Ru and Sr atoms form a near-perfect lattice configuration, agreeing well with previous results conducted on the pure SRO film [22–24], while for the area close to the heterointerface [see area 1 in Fig. 2(b) and Fig. 2(d)], Ru atoms display a considerable offset, leading to the distortion of the RuO_6 oxygen octahedron. The distorted RuO_6 oxygen octahedron results in a reduction of the lattice parameter along the c axis and reflects in the XRD measurements as a satellite SRO-(200) Bragg peak with an increased diffraction angle, consistent with our observations in Fig. 1. As a comparison, we have also checked the cross-section atomic position of the pristine SRO/STO heterostructures at 300 K [i.e., corresponds to the case in Fig. 1(b)]. As shown in Fig. S5 [16], Ru and Sr atoms in the entire SRO layer form the lattice arrangement same as that in area 2 of Fig. 2(b) and no noticeable atomic distortion has been resolved. Such atomic-scale structural information thus suggests that when the STO substrate undergoes the phase transition at 105 K, the octahedral geometry near the interface in the SRO film will be changed and a two-layered structure in the SRO film will be formed.

To further confirm the formation of the two-layered structure in SRO, we probed the lattice dynamics by utilizing ultrafast x-ray diffraction techniques. Briefly, we pump the SRO/STO heterostructure with a femtosecond laser pulse (1.55 eV, 45-fs duration) and after a certain delay time, an ultrashort x-ray pulse (Cu-K_α, ∼ 200-fs duration) is used to probe the photoexcited dynamics in the classical reflection $\theta-2\theta$ geometry. The diffracted x-ray image is recorded by an x-ray charge-coupled device (2048 × 2048 pixels, 13.5-μm pixel size). More details of the home-built UXRD setup are provided in our previous publication [20]. First, we investigate the photoinduced lattice dynamics of the pristine SRO/STO heterostructures at 300 K with a pump fluence of $2\,mJ/cm^2$ (incident fluence). As shown in Figs. 3(a) and 3(b), upon the pump laser reaching the surface of SRO, a transient shift of SRO-(200) Bragg peak towards the lower angle is observed, indicating a fast out-of-plane expansion. The lattice constant increases immediately after photoexcitation, which reaches a maximum, $(\Delta d/d)_{max}$ at $t_{1max} = 11.7$ ps [indicated by a dashed line in Fig. 3(b)]. Subsequently, the expansion of the SRO layer decays to the initial state with the timescale of nanosecond or microsecond. This behavior can be well described as the thermal-like ultrafast photoinduced lattice dynamics based on the two-temperature and linear chain models, i.e., the optical excitation of the metallic SRO layer engenders pronounced temperature gradients, exciting coherent acoustic phonons (strain-wave packets) from the surface. These strain waves propagate into the SRO film with the associated longitudinal sound velocity, modifying the separation of lattice planes and corresponding to the transient Bragg peak shift [25,26]. Based on the characteristic time for the strain wave propagating through the SRO layer (∼ 11.7 ps) and the thickness of the SRO layer (∼ 76.6 nm), the estimated longitudinal sound velocity is about 6.547 nm/ps, which agrees well with the value (∼ 6.312 nm/ps) obtained in the pure SRO film [27].

Photoinduced transient dynamics of SRO/STO at 80 K with a pump fluence of $4\,mJ/cm^2$ are shown in Figs. 3(c) and 3(d). To characterize the dynamic behavior of these two peaks (i.e., one prominent peak at 45.93° and one satellite peak at 46.05°), we fitted the double peaks separately manually to extract peak position change information. As shown in Fig. 3(d), the prominent peak (the green curve) and the satellite peak (the orange curve) exhibit distinct lattice spacing variation dynamics (also see the distinct full width at half maximum and intensity dynamics of these two peaks in Fig. S6) [16], indicating that the SRO (200) Bragg peak is not separated by Cu $K_{\alpha1}$ and Cu $K_{\alpha2}$ lines (i.e., Cu $K_{\alpha1}$ and Cu $K_{\alpha2}$ lines detecting the same lattice plane should show identical dynamics). Meanwhile, there is no dynamic hysteresis for these two peaks in Fig. 3(d), suggesting that the satellite peak shows

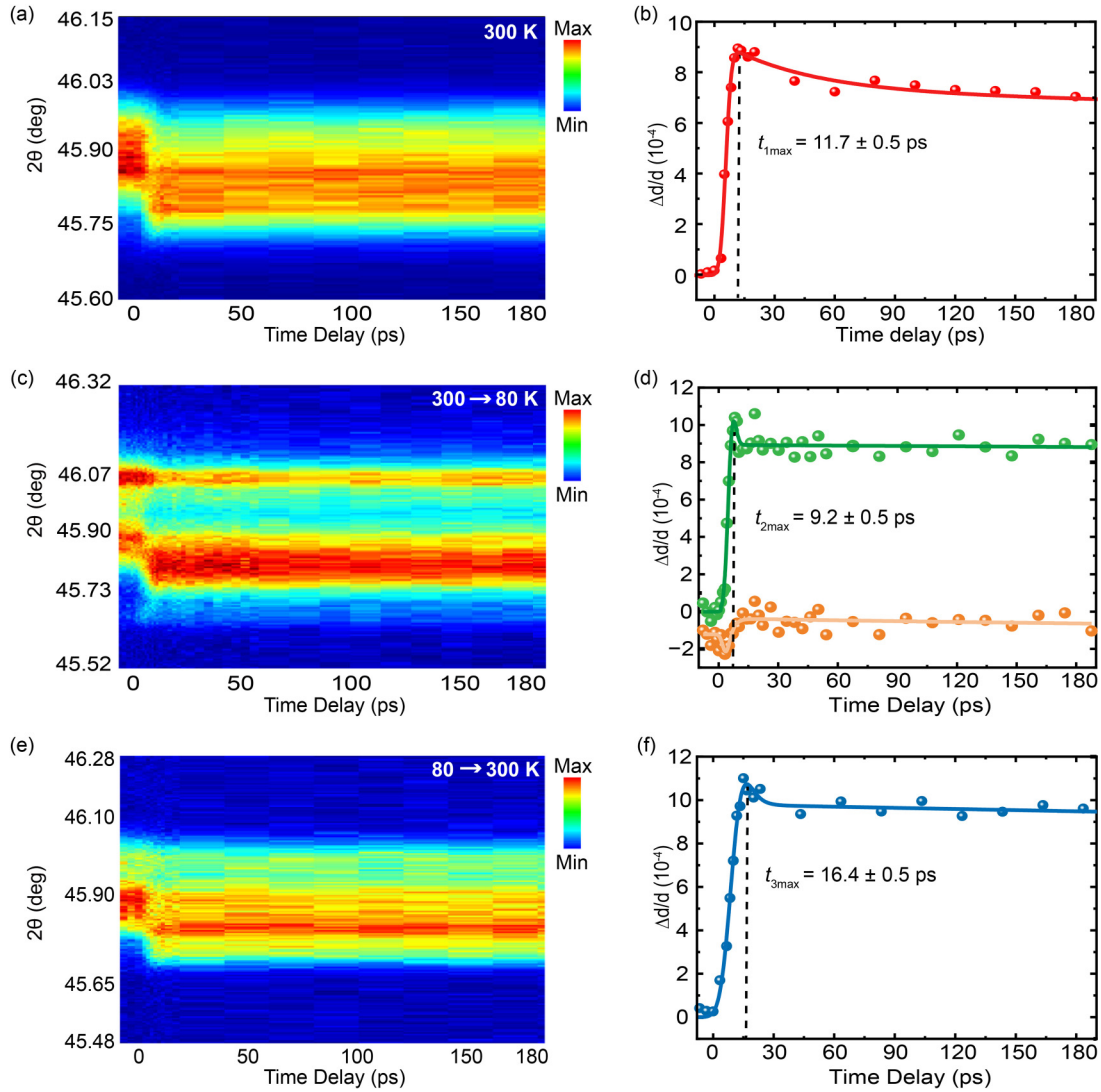

FIG. 3. Ultrafast XRD measurements of the SRO/STO heterostructure with different temperature treatment conditions. (a) Transient $\theta-2\theta$ scans of the SRO (200) Bragg diffraction at 300 K without any cooling history, corresponding to the case in Fig. 1(b). (b) Lattice spacing variation dynamics at 300 K extracted from (a). (c) Transient $\theta-2\theta$ scans of the SRO (200) Bragg diffraction at 80 K, corresponding to the case in Fig. 1(c). (d) Lattice spacing variation dynamics of the prominent peak (the green curve) and the satellite peak (the orange curve) at 80 K extracted from (c). (e) Transient $\theta-2\theta$ scans of the SRO (200) Bragg diffraction at 300 K with the cooling history, corresponding to the case in Fig. 1(d). (f) Lattice spacing variation dynamics at 300 K extracted from (e). The solid lines in (b), (d), and (f) represent exponential fits.

an active dynamic response, that is, the dynamics are caused by the direct laser excitation; otherwise, the propagation of acoustic strain waves in the passive dynamic process (i.e., the dynamics due to the strain-wave propagation) should lead to an apparent hysteresis [25,26,28]. Based on these facts, therefore, we can safely conclude that the origin of the satellite peak is due to the formation of a two-layered structure in the SRO film and the thickness of each layer can be well determined. Similar to the analysis in Figs. 3(a) and 3(b), with the characteristic time $t_{2max} = 9.2$ ps the estimated thickness of the unchanged and distorted SRO layer is 60.2 and 16.4 nm, respectively. Please note that t_{2max} of the prominent peak persists as the pump fluence increases to 8 mJ/cm^2 (see Fig. S7) [16], further implying that the two-layered structure in the SRO film is linked to the phase transition of the STO substrate below 105 K instead of the optical laser excitations [26].

We have also noticed that the satellite peak in Fig. 3(d) exhibits initial bipolar stress switching at early time delays (i.e., compression first and then expansion), in contrast to the quasi-instantaneous expansion of the prominent peak. As reported in previous studies [26,29], the excitation spatial profile strongly correlates with the shape factor $\delta = d/\zeta$, where d is the layer thickness and ζ denotes the optical penetration depth. The bipolar stress switching observed here indicates that $\delta >> 1$ in the distorted SRO layer (i.e., the laser penetration depth is slightly larger than the thickness of the unchanged SRO layer, which can only excite a small fraction of the distorted SRO layer). Under this condition, the nonuniform excitation causes the excited part of the distorted SRO layer to expand and compress the unexcited part, which results in a different strain profile compared to the unchanged SRO layer [26]. In addition, Figs. 3(e) and 3(f)

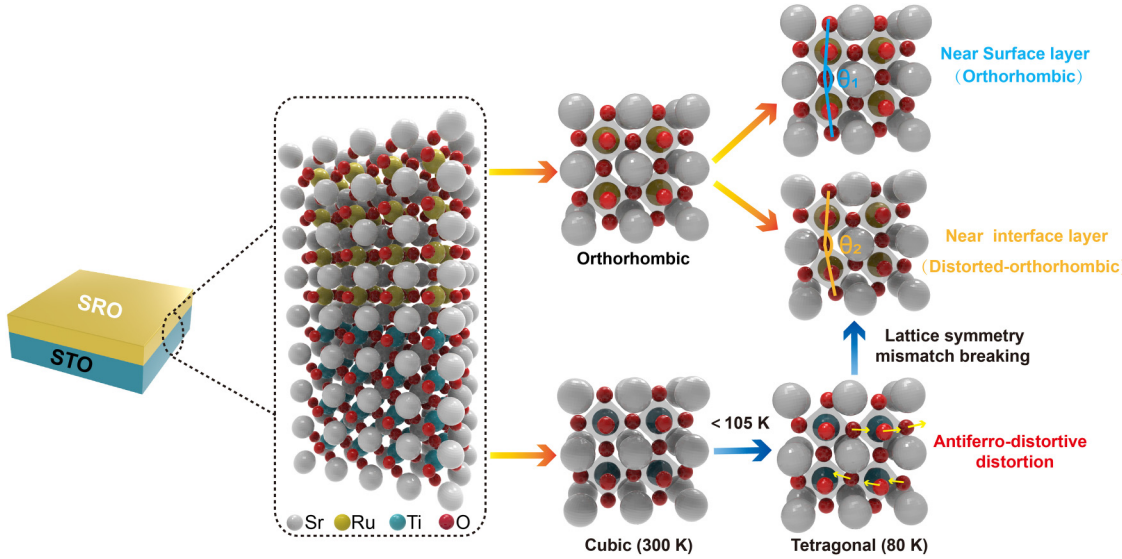

FIG. 4. A schematic illustration of the interface lattice reconstruction in SRO/STO heterostructures triggered by the structural transition of STO at low temperature (< 105 K). (100) SRO film with an orthorhombic unit cell is deposited on (100) STO substrate. Below 105 K, the STO substrate undergoes a cubic-to-tetragonal transition, leading to the breaking of interface lattice symmetry mismatch and the formation of a two-layered structure in the SRO film. One is the near-surface layer, which remains the orthorhombic structure, and the other is the near-interface layer, with a larger tilt angle of RuO_6 octahedral relative to the initial layer.

depicts the photoinduced lattice dynamics of SRO/STO at 300 K under the same pump fluence ($4\,mJ/cm^2$) with a cooling history [corresponding to the case in Fig. 1(d)]. In this case, accurately distinguishing the dynamic process of the satellite peak is challenging due to the obscure satellite peak [see the static x-ray-diffraction pattern in Fig 1(d)]. Thus, the photoinduced transient dynamics described here contain contributions from both the residual satellite and the prominent peak. Based on the characteristic time $t_{3max} = 16.4$ ps, the estimated longitudinal acoustic velocity is 4.67 nm/ps, which is reduced by approximately 30% compared to the value in the pure SRO film. Therefore, the contribution from the residual satellite peak cannot be neglected. Similar to Figs. 3(e) and 3(f), we have also checked the pump-dependent maximum lattice change $(\Delta d/d)_{max}$ and the characteristic time of SRO/STO at 300 K with a cooling history. As shown in Fig. S8 [16], $(\Delta d/d)_{max}$ is positively and linearly correlated with increasing fluences while t_{3max} remains unchanged, confirming again the observed dynamic process is a thermal-like behavior [30] and ruling out any change of the longitudinal acoustic velocity caused by nonthermal factors. Please note that the excitation fluence used in three conditions are different [i.e., $2\,mJ/cm^2$ in Fig. 3(a) and $4\,mJ/cm^2$ in Figs. 3(c) and 3(e)] since for the pristine state at 300 K, previous UXRD measurements [25,26] have demonstrated that the characteristic times (longitudinal sound velocity) are independent of the fluence change.

Based on the experiment results, we have schematically illustrated the interfacial lattice reconstruction in the SRO/STO heterostructure triggered by the structural transition of STO, as shown in Fig. 4. The epitaxial SRO film in the SRO/STO heterostructure experiences in-plane compressive strain, resulting in an orthorhombic structure at room temperature with slight tilting and rotation of the RuO_6 octahedra [31,32]. Below 105 K, the STO substrate undergoes an antiferroelectric distortion phase transition (from cubic to tetragonal phase), leading to a decrease in the lattice constant a and an increase in the lattice constant c due to the rotation of TiO_6 octahedra in neighboring unit cells [12,14,33]. This results in an intensified lattice mismatch at the interface, causing notably compressive strain. Previous research indicates that this reduction in lattice symmetry of the STO substrate below 105 K affects the symmetry of the adjacent $La_{2/3}Ca_{1/3}MnO_3$ lattice [9], as demonstrated by a martensitic transition from the tetragonal to the orthorhombic phase. At 80 K, the SRO film bifurcates into a "near-interface layer" and a "near-surface layer". As the film thickness increases, the strain introduced by the substrate tends to relax, and the lattice structure of the near-surface layer tends to revert to a bulklike structure [32,34]. The structural transition of the STO substrate introduced a further tilted distortion in the RuO_6 octahedra of the near-interface layer, with a scale of up to 16.4 nm. Meanwhile, in the case of 300 K with cooling history, the persistence of the distorted state primarily results from excessive interface stress mismatch induced by the phase transition of STO substrates. This results in irreversible minor damage and a substantial softening of the oxygen octahedral lattice in the epitaxial SRO layer. We predict that 100% of the SRO layer will be distorted if the SRO thickness is even thinner, owing to the strong stress mismatch near the interface. Theoretical calculations indicate that the RuO_6 octahedral network near the interface in the SRO/STO heterostructure exhibits remarkable rigidity, with the interface layer maintaining a size smaller than 1 unit cell [35]. However, during epitaxial growth, an enlargement of the transition-layer size is observed (9 to 18 unit cells) due to the temperature-dependent orthorhombicity factor [31]. This enlargement accommodates greater distortions and alleviates stress caused by the lattice mismatch. Consequently, the RuO_6 octahedral network softens, leading to a reduction in longitudinal acoustic velocity. The local magnetism of SRO, strongly influenced by the hybridization

between the Ru d orbitals and the O p orbitals, is highly sensitive to symmetry changes induced by disruptions in local symmetries [35–38]. By modulating the strain imposed by the substrate, a multilayer magnetic structure and associated magnetic phase transitions can emerge, similar to the observation of twinning in $La_{1-x}Sr_xMnO_3$ ($x = 0.175$) thin films on an STO substrate at 105 K, which exhibit a three-layer magnetic distribution [10]. The SRO/STO heterostructure is frequently used in transistor-like structures, where strain engineering can enhance the performance of adjacent functional films (such as $BiFeO_3$ and $PbZr_{0.52}Ti_{0.48}O_3$) [39,40]. The two-layered structure within the SRO film offers possibilities for magnetoelectric effects, electronic memory, and logic devices [41–44].

III. CONCLUSIONS

In conclusion, our study provides a comprehensive understanding of the microscopic mechanism underlying the lattice structure reconstruction observed in SRO films during the cubic-to-tetragonal transition of the STO substrate. Through high-resolution atomic-scale imaging of the RuO_6 octahedral, we have directly observed the distortion of the octahedral structure, characterized by larger tilt angles, at the SRO/STO interface following a cooling history. Additionally, employing acoustic phonon strain-wave propagation analysis at temperatures of 80 and 300 K, we have discovered the formation of a distinct two-layered structure within the SRO film. This intriguing phenomenon can be attributed to the cubic-to-tetragonal transition experienced by the STO substrate, which stimulates the lattice reconstruction phenomenon in the SRO film. The importance of our research lies in its contribution towards unraveling the reconstructed octahedral network and uncovering a ground state within a single epitaxial SRO film resulting from the structural transformation of the STO substrate.

ACKNOWLEDGMENTS

This work was supported by the National Natural Science Foundation of China (Grant No. 52072324), Science Challenge Project (Grant No. TZ2018001), and Project of State Key Laboratory of Environment-friendly Energy Materials, Southwest University of Science and Technology (Grant No. 22fksy06).

[1] A. Ohtomo and H. Y. Hwang, A high-mobility electron gas at the $LaAlO_3/SrTiO_3$ heterointerface, Nature (London) **427**, 423 (2004).

[2] J. H. Haeni, P. Irvin, W. Chang, R. Uecker, P. Reiche, Y. L. Li, S. Choudhury, W. Tian, M. E. Hawley, B. Craigo *et al.*, Room-temperature ferroelectricity in strained $SrTiO_3$, Nature (London) **430**, 758 (2004).

[3] A. Y. Abid, Y. Sun, X. Hou, C. Tan, X. Zhong, R. Zhu, H. Chen, K. Qu, Y. Li, M. Wu *et al.*, Creating polar antivortex in PbTiO3/SrTiO3 superlattice, Nat. Commun. **12**, 2054 (2021).

[4] G. Koster, L. Klein, W. Siemons, G. Rijnders, J. S. Dodge, C.-B. Eom, D. H. A. Blank, and M. R. Beasley, Structure, physical properties, and applications of $SrRuO_3$ thin films, Rev. Mod. Phys. **84**, 253 (2012).

[5] Q. Qin, L. Liu, W. Lin, X. Shu, Q. Xie, Z. Lim, C. Li, S. He, G. Chow, and J. Chen, Emergence of topological Hall effect in a $SrRuO_3$ single layer, Adv. Mater. **31**, 1807008 (2019).

[6] Y. J. Ma, T. R. Xia, and W. B. Wang, Visualization of ferromagnetic domains in vanadium-doped topological insulator thin films and heterostructures, Tungsten **5**, 288 (2023).

[7] W. Wang, M. W. Daniels, Z. Liao, Y. Zhao, J. Wang, G. Koster, G. Rijnders, C. Chang, D. Xiao, and W. Wu, Spin chirality fluctuation in two-dimensional ferromagnets with perpendicular magnetic anisotropy, Nat. Mater. **18**, 1054 (2019).

[8] K. Y. Meng, A. S. Ahmed, M. Baćani, A. Mandru, X. Zhao, N. Bagués, B. Esser, J. Flores, D. McComb, H. Hug *et al.*, Observation of nanoscale skyrmions in $SrIrO_3/SrRuO_3$ bilayers, Nano Lett. **19**, 3169 (2019).

[9] V. Vlasko-Vlasov, Y. K. Lin, D. J. Miller, U. Welp, G. Crabtree, and V. Nikitenko, Direct magneto-optical observation of a structural phase transition in thin films of manganites, Phys. Rev. Lett. **84**, 2239 (2000).

[10] X. Li, J. Han, X. Zhang, R. Wu, Y. Zhang, H. Tian, M. Xue, X. Wen, Z. Li, S. Liu *et al.*, Non-synchronized rotation of layered spin configurations in $La_{0.825}Sr_{0.175}MnO_3/SrTiO_3$ film, Acta Mater. **181**, 470 (2019).

[11] M. Egilmez, M. M. Saber, I. Fan, K. H. Chow, and J. Jung, Correlation of structural phase transition and electrical transport properties of manganite films on $SrTiO_3$, Phys. Rev. B. **78**, 172405 (2008).

[12] G. Shirane and Y. Yamada, Lattice-dynamical study of the 110 K phase transition in $SrTiO_3$, Phys. Rev. **177**, 858 (1969).

[13] T. Koga, Z. Lu, K. Munakata, M. Hatakeyama, Y. Soejima, and A. Okazaki, Domain population in $SrTiO_3$ below the cubic-to-tetragonal phase transition, Phase Transit. **54**, 109 (1995).

[14] R. Loetzsch, A. Lübcke, I. Uschmann, E. Förster, V. Große, M. Thuerk, T. Koetting, F. Schmidl, and P. Seidel, The cubic to tetragonal phase transition in $SrTiO_3$ single crystals near its surface under internal and external strains, Appl. Phys. Lett. **96**, 071901 (2010).

[15] D. J. Singh, Electronic and magnetic properties of the 4d itinerant ferromagnet $SrRuO_3$, J. Appl. Phys. **79**, 4818 (1996).

[16] See Supplemental Material at http://link.aps.org/supplemental/10.1103/PhysRevB.108.224113 for the detailed lattice structures of the SRO film and the STO substrate; XRD patterns of the SRO/STO heterostructures acquired with a standard commercial diffractometer and acquired from PXS at 120 K; static diffraction simulation of SRO/STO; comprehensive experimental parameters for structural characterization; high-resolution TEM image of the cross-section atomic position of the pristine SRO/STO heterostructures at 300 K; other related ultrafast x-ray-diffraction measurements of SRO /STO heterostructures at 80 K; photoinduced transient dynamics of SRO/STO at 80 K with higher pump fluence; and photoinduced transient dynamics of SRO/STO at 300 K (with cooling history) with higher pump fluence. The Supplemental Material also contains Refs. [4,17–20,25,28].

[17] C. W. Jones, P. D. Battle, P. Lightfoot, and W. T. A. Harrison, The structure of $SrRuO_3$ by time-of-flight neutron powder diffraction, Acta Crystallogr. Sect. C **45**, 365 (1989).

[18] F. W. Lytle, X-ray diffractometry of low-temperature phase transformations in strontium titanate, J. Appl. Phys. **35**, 2212 (1964).

[19] P. A. Fleury, J. F. Scott, and J. M. Worlock, Soft phonon modes and the 110 K phase transition in $SrTiO_3$, Phys. Rev. Lett. **21**, 16 (1968).

[20] D. Zhao, P. You, J. Yang, J. Yu, H. Zhang, M. Liao., and J. Hu., A highly stable-output kilohertz femtosecond hard x-ray pulse source for ultrafast x-ray diffraction, Appl. Sci. **12**, 4723 (2022).

[21] N. Higashi, T. Watanabe, K. Saito, I. Yamaji, T. Akai, and H. Funakubo, Crystal structure comparison between conductive $SrRuO_3$ and $CaRuO_3$ thin films, J. Cryst. Growth. **229**, 450 (2001).

[22] H. Wang, G. Laskin, W. He, H. Boschker, M. Yi, J. Mannhart, and P. A. van Aken, Tunable magnetic anisotropy in patterned $SrRuO_3$ quantum structures: Competition between lattice anisotropy and oxygen octahedral rotation, Adv. Funct. Mater. **32**, 2108475 (2022).

[23] Z. Liao, M. Huijben, Z. Zhong, N. Gauquelin, S. Macke, R. J. Green, S. Van Aert, J. Verbeeck, G. Van Tendeloo, K. Held, G. A. Sawatzky, G. Koster, and G. Rijnders, Controlled lateral anisotropy in correlated manganite heterostructures by interface-engineered oxygen octahedral coupling, Nat. Mater. **15**, 425 (2016).

[24] Y. Gu, Y.-W. Wei, K. Xu, H. Zhang, F. Wang, F. Li, M. S. Saleem, C.-Z. Chang, J. Sun, and C. Song, Interfacial oxygen-octahedral-tilting-driven electrically tunable topological Hall effect in ultrathin $SrRuO_3$ films, J. Phys. D: Appl. Phys. **52**, 404001 (2019).

[25] D. Schick, A. Bojahr, M. Herzog, P. Gaal, I. Vrejoiu, and M. Bargheer, Following strain-induced mosaicity changes of ferroelectric thin films by ultrafast reciprocal space mapping, Phys. Rev. Lett. **110**, 095502 (2013).

[26] D. Schick, M. Herzog, A. Bojahr, W. Leitenberger, A. Hertwig, R. Shayduk, and B. Matias., Ultrafast lattice response of photoexcited thin films studied by X-ray diffraction, Struct. Dyn. **1**, 064501 (2014).

[27] S. Yamanaka, T. Maekawa, H. Muta, T. Matsuda, S. Kobayashi, and K. Kurosaki, Thermophysical properties of $SrHfO_3$ and $SrRuO_3$, J. Solid State Chem. **177**, 3484 (2004).

[28] C. V. Korff Schmising, M. Bargheer, M. Kiel, N. Zhavoronkov, M. Woerner, T. Elsaesser, I. Vrejoiu, D. Hesse, and M. Alexe, Strain propagation in nanolayered perovskites probed by ultrafast x-ray diffraction, Phys. Rev. B **73**, 212202 (2006).

[29] B. B. Zhang, J. Liu, X. Wei, D. Sun, Q. Jia, Y. Li, and Y. Tao, Photoinduced coherent acoustic phonon dynamics inside Mott insulator Sr_2IrO_4 films observed by femtosecond X-ray pulses, Appl. Phys. Lett. **110**, 151904 (2017).

[30] H. Zhang, Y. Zhang, R. Li, J. Yu, W. Dong, C. Chen, K. Wang, X. Tang, and J. Chen, Room temperature hidden state in a manganite observed by time-resolved X-ray diffraction, npj Quantum Mater. **4**, 31 (2019).

[31] W. Lu, P. Yang, W. D. Song, G. M. Chow, and J. S. Chen, Control of oxygen octahedral rotations and physical properties in $SrRuO_3$ films, Phys. Rev. B **88**, 214115 (2013).

[32] S. H. Chang, Y. J. Chang, S. Y. Jang, D. W. Jeong, C. U. Jung, Y.-J. Kim, J.-S. Chung, and T. W. Noh, Thickness-dependent structural phase transition of strained $SrRuO_3$ ultrathin films: The role of octahedral tilt, Phys. Rev. B **84**, 104101 (2011).

[33] S. A. Hayward and E. K. H. Salje, Cubic-tetragonal phase transition in $SrTiO_3$ revisited: Landau theory and transition mechanism, Phase Transit. **68**, 501 (1999).

[34] C. U. Jung, H. Yamada, M. Kawasaki, and Y. Tokura, Magnetic anisotropy control of $SrRuO_3$ films by tunable epitaxial strain, Appl. Phys. Lett. **84**, 2590 (2004).

[35] J. He, A. Borisevich, S. V. Kalinin, S. J. Pennycook, and S. T. Pantelides, Control of octahedral tilts and magnetic properties of perovskite oxide heterostructures by substrate symmetry, Phys. Rev. Lett. **105**, 227203 (2010).

[36] W. Lu, W. Dong Song, K. He, J. Chai, C. J. Sun, G.-M. Chow, and J.-S. Chen, The role of octahedral tilting in the structural phase transition and magnetic anisotropy in $SrRuO_3$ thin film, J. Appl. Phys. **113**, 063901 (2013).

[37] S. Lin, Q. Zhang, M. A. Roldan, S. Das, T. Charlton, M. R. Fitzsimmons, Q. Jin, S. Li, Z. Wu, S. Chen *et al.*, Switching magnetic anisotropy of $SrRuO_3$ by capping-layer-induced octahedral distortion, Phys. Rev. Appl. **13**, 034033 (2020).

[38] W. Lu, W. Song, P. Yang, J. Ding, G. M. Chow, and J. Chen, Strain engineering of octahedral rotations and physical properties of $SrRuO_3$ films, Sci. Rep. **5**, 10245 (2015).

[39] H. W. Jang, S. H. Baek, D. Ortiz, C. M. Folkman, R. R. Das, Y. H. Chu, P. Shafer, J. X. Zhang, S. Choudhury, V. Vaithyanathan *et al.*, Strain-induced polarization rotation in epitaxial (001) $BiFeO_3$ thin films, Phys. Rev. Lett. **101**, 107602 (2008).

[40] W. Gao, L. You, Y. Wang, G. Yuan, Y.-H. Chu, Z. Liu, and J.-M. Liu, Flexible $PbZr_{0.52}Ti_{0.48}O_3$ capacitors with giant piezoelectric response and dielectric tunability, Adv. Electron. Mater. **3**, 1600542 (2017).

[41] J. Zhou, X. Shu, W. Lin, D. Shao, S. Chen, L. Liu, P. Yang, E. Tsymbal, and J. Chen, Modulation of spin–orbit torque from $SrRuO_3$ by epitaxial-strain-induced octahedral rotation, Adv. Mater. **33**, 2007114 (2021).

[42] J. Yu, Y. Han, L. Wang, Y. Liu, and J. Hu, Metal−organic framework-based ultrafast logic gates for high-security optical encryption, Ultrafast Sci. **3**, 0030 (2023).

[43] G. Tian, F. Zhang, J. Yao, H. Fan, P. Li, Z. Li, X. Song, X. Zhang, M. Qin, M. Zeng *et al.*, Magnetoelectric coupling in well-ordered epitaxial $BiFeO_3/CoFe_2O_4/SrRuO_3$ heterostructured nanodot array, ACS Nano **10**, 1025 (2016).

[44] K. Q. Geng, M. Q. Yang, J. X. Meng, L.-F. Zhou, Y.-Q. Wang, S. Dmytro, Q. Zhang, S.-W. Zhong, and Q.-X. Ma, Engineering layered/spinel heterostructure via molybdenum doping towards highly stable Li-rich cathodes, Tungsten. **4**, 323 (2022).